ENGINEERING AND INDUSTRIAL EXPERIMENT STATION

College of Engineering

University of Florida

Gainesville

Ninth Semiannual Report

A STUDY OF DEFECT STRUCTURES WITH THE FIELD-ION MICROSCOPE

NASA Research Grant
NGR-10-005-039

Submitted to:

National Aeronautics and Space Administration

Submitted by:

Deaprtment of Metallurgical and Materials Engineering
University of Florida
Gainesville, Florida

J. J. Hren, Chief Investigator
U. T. Son, Post Doctoral Fellow
D. Stoltz, Graduate Assistant
T. Headley, Graduate Assistant

For the Period

March 1, 1970 - August 31, 1970

I. INTRODUCTION

Progress in the past report has been centered about three areas: (1) development and operation of the atom probe field-ion microscope, (2) optical transforms of field-ion micrographs and (3) field-ion microscopy of Cu-Au alloys.

The atom probe has been assembled, however, there were some difficulties due to the leak in the system. The specimen manipulation mechanism was redesigned to correct the leak in the system and primiary atom probe run with Iridium specimen was carried out. These results are included in this report with detailed structure of atom probe field-ion microscope.

Fraunhofer diffraction patterns of ideal field-ion micrographs and actual field-ion micrographs of an ordered alloy have been obtained to evaluate quantitatively the long-range order parameter. A computer simulated field-ion image was used as an ideal mask to establish a relationship between the number of image points and the intensities of the concentric rings of the rotated diffraction pattern. The actual field-ion micrographs obtained from different ordered states of 50 atomic per cent FePt alloy have been used as a mask for the optical transform. The integrated intensities of the concentric rings of rotated diffraction patterns were used to evaluate the long-range order parameter and the results are compared with data obtained by other methods. Some factors contributing to the discrepancy between ideal and experimental cases are investigated.

Field-ion images of near stoichiometric AuCu and $AuCu_3$ alloys have been obtained using a 3 inch channel plate image intensifier. The field-ion image of fully ordered $AuCu_3$ alloy

appeared unstable and irregular initially, however, a regular image was obtained after field evaporation of the surface layers. The hellium ion image was obtained only with the channel plate image intensifier, but the hydrogen ion image was obtained without the image intensifer. The advantage of the channel plate image intensifier is not only the intensity gain but also the reduction of gas impact effect on the field evaporation by lowering the operating pressure of the imaging gases. Further studies on the ordering kinetics of $AuCu_3$ alloy will be conducted using direct counting and optical transform method and the results will be compared with the results obtained by conventional techniques (resistivities, x-ray). A more complete report on the study of $AuCu_3$ should be available in March, 1971.

II. OPTICAL TRANSFORMS OF FIELD-ION MICROGRAPHS

A. Introduction

The Fourier method of producing an electron density map from x-ray diffraction data in a purely analytical way is widely used, however, this method requires considerable mathematical skill and effort. In 1939, Bragg (1) suggested that an image of the structure could be built up by superimposing fringes photographically. This technique is called an optical transform or a Fourier synthesis. Its use for crystal structure determination was first suggested by Ewald (2) and Knott (3) in 1940. Since then the optical transform technique has been applied to a large variety of x-ray scattering problems. For example: the initial phase problem in single crystal work, problems of crystallinity in fibers and other materials (e.g., Hosemann (4)), and the study of diifuse scattering. Applications of optical transforms outside the field of x-ray diffraction are also numerous; for example, as an aid to: the interpretation of electron micrographs, as shown by Klug and Burger (5); the interpretation of aireal photos, or even the speedy recording of individual finger prints in quantity (6).

In the present paper we use this technique as a tool to interpret field-ion micrographs of fully ordered and partially ordered alloys. The precise determination of the atomic occupational fraction, or the long-range order parameter, from field-ion studies is possible using direct counting method (7) provided only a single species contributes to the image. However, the direct counting method requires large numbers of micrographs and image points for reasonable statistical significance and this is time consuming and tedious.

The primary information in which we are interested in order to determine atomic order parameters is the number of image points on right and wrong sites. There are no available theories or experimental data with which the Fraunhofer diffraction pattern of a field-ion image can be adequately interpreted for this purpose. Therefore, we conducted a series of experiments to find any useful correlations between the parameters of the optical mask and the parameters on the Fraunhofer diffraction pattern. Our first attempts with experimental field-ion images as the imput masks yielded very complicated Fraunhofer diffraction patterns, consequently, a simplified study was first carried using ideal field-ion images generated by computer simulation. Once having established useful empirical relations for the ideal image, these results were used to evaluate the long-ranger order parameters from experimental images of an FePt alloy.

B. Experimental Technique

The beam path of the optical diffractometer is shown in Fig. 1. A Helium Neon 200 watt laser generator is the source of the beam. The laser beam is directed through a condenser and bent by a prism; Point B is a secondary source, the pin hole; C and D are the main lenses; O is the location of the mask; E is the mirror; F is the back focal plane of D in which the final pattern is observed by a microscope or in which the film is placed for photographic recording.

It is not essential that the main lenses C and D be identical. It is not in fact even necessary to have two lenses; in principle, one lens of half the focal length would suffice with the mask placed immediately above or below it. However, the symmetrical system of two lenses is preferred because it permits more satisfactory correction for spherical abberation.

There are three steps to obtain useful data from an optical transform of a field-ion micrograph. These are the mask preparation, the optical transform and the microdensitometer reading. All the masks were prepared photographically. A negative field-ion micrograph was placed on a light box and a portion of the micrograph was recorded on a high contrast 35mm film with a copy camera. The field-ion image points which appear as dark spots on the negative give transparent points as the end product of the copy camera. In order to obtain substantially identical masks from different portions of a micrograph all the photographic parameters were kept constant. For computer simulated images (Fig. 2(a)) the negatives were used directly as masks.

Fraunhofer diffraction patterns were obtained from the diffractometer shown in Fig. 1. Two types of Fraunhofer diffraction patterns were obtained namely, stationary and rotated. The former is obtained by keeping the mask stationary through the exposure of the diffraction pattern; the latter is obtained by rotating the mask during exposure. The stationary pattern (Fig. 2 (b)) was useful for a qualitative analysis, however, the rotated pattern (Fig. 2 (c)) was more useful for quantitative analysis. If the object in real space is rotated in a given sense and a given angular velocity, the transform will rotate in the same sense at the same angular velocity. However, it is important to recognize that the location of the axis of rotation in real space is not critical; the rotation in reciprocal space is always about a parallel axis through the center.

The final quantitative data from a rotated diffraction pattern was obtained using a microdensitometer. A rotated diffraction pattern which was recorded on a 35 mm film was placed under 10X eye piece and the intensity variation recorded using 100-1 lever arm ratio. From

this microdensitometer reading the separation of intensity maxima peaks and the integrated intensities of each peak were measured.

C. Experimental Results

The object of this study was to find a correlation between the number of image points and the intensity of the corresponding maxima while isolating the diffraction effects due to misplaced image points from the Fraunhofer diffraction pattern.

In order to establish a method of identifying the intensity maxima, a well resolved high index plane of Ni_4Mo containing 18 image points was used as a first mask. The distance and frequency from one image point to all others were measured and are tabulated in Table 1. The corresponding plot of distance versus frequency is plotted in Fig. 3. Five distinct groups (V, W, X, Y, Z) are detected from this plotting. However, the separation between the three groups X, Y, and Z is so small that they are considered as a single group. The rotated diffraction pattern was obtained from this mask and a microdensitometer reading obeyed the following simple relation.

$$d = \frac{K}{D} \qquad (1)$$

Where d is the separation of image points in the real space and D is the separation of the intensity maxima peak on a diffraction pattern and K is a constant.

An experimental field-ion micrograph contains some geometric distortion due to the projection geometry, but a simulated image can be considered disregarding this geometric distortion. A superlattice plane of a fully ordered A B type or L1 type alloy is shown in Fig. 4. The circles with dots in the center indicate ideal field-ion image points.

Assuming only one species contributes to the image points, the misplaced atoms which are located on wrong sites can be evaluated using the lattice vector relationships as shown in Fig. 4 and equation (1).

Suppose $\vec{d}_1$, $\vec{d}_2$, $\vec{d}_1^*$ and $\vec{d}_2^*$ are position vectors describing B atoms on right sites and wrong sites from the same arbitrary orgin, and D_1, D_2, and D_1^* and D_2^* are the corresponding separations of the intensity maxima in a diffraction pattern. Then the following relationships apply

$$D_1 = \frac{K}{d_1} \qquad \text{where } d_1 = m\vec{a} + m\vec{b}$$

$$D_2 = \frac{K}{d_2} \qquad d_2 = h\vec{a} + k\vec{b}$$

$$D_1^* = \frac{K}{d_1^*} \qquad d_1^* = n\vec{a}' + m\vec{b}'$$

$$D_2^* = \frac{K}{d_2^*} \qquad d_2^* = h\vec{a}' + k\vec{b}'$$

where n, m, h and k are integers and $\vec{a}$, $\vec{b}$ and $\vec{a}'$ $\vec{b}'$ are unit vectors.

$$\frac{D_1}{D_2} = \frac{d_2}{d_1} = \frac{\sqrt{h^2 + k^2}}{\sqrt{n^2 + m^2}} \tag{2}$$

$$\frac{D_1^*}{D_2^*} = \frac{d_2^*}{d_1^*} = \frac{\sqrt{h^2 + k^2}}{\sqrt{n^2 + m^2}} \tag{3}$$

$$\frac{D_1}{D_2^*} = \frac{d_2^*}{d_1} = \frac{\sqrt{h^2 + k^2}}{\sqrt{2}\sqrt{n^2 + m^2}} \tag{4}$$

From these equations it is clear that any intensity maxima peak contributed by misplaced image points (due to the misplaced atoms with sites on wrong atomic sites) can be sorted out or identified by taking

the ratio as given in equation (4). The ratio contains a factor of $\frac{1}{\sqrt{2}}$. It should be kept in mind that the ratio of $\frac{1}{\sqrt{2}}$ can be obtained for the normal ratio given by equations (2) and (3). However, this confusion can be easily removed by comparing with the diffraction pattern of a fully ordered micrograph, which does not contain misplaced image points.

Once the peaks are identified by their separation, the next step is the evaluation of the integrated intensity. Although it is possible to obtain considerable information from the Fraunhofer diffraction pattern, analytically this approach can often be carried out only approximately. It is therefore useful to establish an empirical correlation between the transform of an ideal image and the number and disposition of image points. Several diffraction patterns similar to Fig. 2 were obtained with masks made from different portions of the computer simulated image. These are shown in Fig. 5 (a), (b), (c). Clearly the symmetry and over all shape of the image affects the stationary diffraction pattern, however, rotated patterns are all qualitatively similar. The most useful diffraction patterns were obtained from masks having centro symmetry as in Fig. 2. Emperical relationships were obtained by changing the number of image points on the mask of Fig. 2 from 100% to 80, 60, and 50%, corresponding to a change from full order to randomness and the integrated intensities of the corresponding Fraunhofer diffraction patterns compared and measured. Such changes in the number of image points was detected as a change of intensity with an error limit of $\pm 4\%$. From these results the following empirical relationship between intensity and the occupation fraction of A atoms on the superlattice sites was established:

$$\frac{I_o}{I_n} = \frac{r_\alpha}{X_A} \tag{5}$$

where I_o is the integrated intensity of the central maxima of the Fraunhofer diffraction pattern, r_α is the fraction of A atoms on right sites. $I_n = I_o$ when $r_\alpha = X_A$ (random case).

Therefore,

$$r_\alpha = X_A \frac{I_o}{I_n} \tag{6}$$

or

$$r_\alpha = \frac{I_o}{I_p} \tag{7}$$

where $I_p = I_o$ when $r_\alpha = 1$ (fully ordered). It is possible to evaluate an occuaptional fraction r_α using equations (6) and (7). Equation (7) is most useful in practice.

The methods just described were applied to the FePt system. Figure 6 shows a typical mask and the corresponding diffraction pattern. Other field-ion images of partially ordered FePt were also obtained and used to evaluate their respective long-range order parameters. Specimens were heat treated to approach equilibrium at 1200°C, 900°C and 475°C and the long-range order parameters of these specimens were also evaluated by x-ray methods and by direct counting (7). These data are compared with the present optical transform method. The (001) pole of each micrograph was used as a mask for the optical transform and the long-range order parameter evaluated according to equation (7). Table II gives a comparison of the data obtained by x-ray methods, direct counting (8) and optical transforms as described above. The

theoretical values of Bragg and Williams (9) and Cowley (10) are also listed for comparison. The significance of this data in understanding the mechanism of atomic ordering in these alloys is discussed at length in a separate paper. We are interested here only in evaluating optical transforms as a means of gathering quantitative data. In general the transform method compares to within ±6% with the direct counting technique. However, there are several important factors, qualifications required to obtain reasonable quantitative data from an optical transform of an experimental field-ion micrograph. These are listed not necessarily in order of importance.

(1) It is assumed that only one species (on right or wrong sites) contributes to the image points.

(2) The effect of local distortion of the field-ion image due to the projection must be minimized for best results.

(3) Each image point should represent just one atomic site, and the size of all image points should be uniform.

(4) Centro-symmetric regions of the field-ion micrograph are best employed.

(5) All photographic variables must be kept as constant as possible throughout the experimental steps.

D. Conclusions

Using computer simulated field-ion micrographs, two important empirical equations are defined and justified. These results are found to be very useful in evaluating the long-range order parameter of ordered alloys of Fe and Pt from field-ion micrographs. The results agreed with direct counting methods within ±6%. Therefore, optical transform techniques, which were orginally found useful in interpreting x-ray phenomenon, are also useful in field-ion microscopy of ordered alloys.

III. FIELD-ION MICROSCOPY OF ORDERD Cu-Au ALLOY

Alloys of copper and gold were among the first to be recognized as possessing atomic order and have been extensively studied since by a variety of experimental techniques. (11-15) None of the methods used so far, however, has been capable of measuring atomic order parameters locally, but rather depended on the interpretation of bulk averages. In recent years the field-ion microscope has been shown capable of providing order parameters in several alloys by direct counting or by optical transformation of field-ion micrographs. (7,8) Unfortunately, alloys of nonrefractory metals are rather difficult to study by FIM, although several investigators have obtained at least metastable images. (16-18) The chief difficulties are associated with: (i) the marginal stability of these alloys to field evaporation, (ii) the differentiation of atomic species, and (iii) the methods of measuring order parameters with reasonable counting statistics. We report here our method for overcoming these difficulties for near stoichiometric CuAu and Cu_3Au. A subsequent paper will describe in detail the results of the studies on the ordering process itself.

The process of specimen preparation for field-ion microscopy is not complete until a stable field-evaporation end form has been obtained. In turn, this end form is at least partly dependent upon the prior tip shaping operations--generally by chemical or electro-chemical etching. The ideal tip shaping procedure prior to field evaporation would yield approximately a hemisphere merging into a smoothly tapered cone of circular cross section. Furthermore, the tip's structure should not be altered by the shaping operation--e.g., by deformation or by atomic diffusion. Since the sought for tip radius is $\lesssim 0.1\mu m$, it cannot be resolved by light optical methods.

The following tip-shaping steps prior to field evaporation were successful in overcoming the above difficulties for CuAu and Cu_3Au. (1) The initial specimen cross section was made as close to circular as possible. (2) An Electrochemical solution was chosen that gave a high polish with a relatively-low rate of removal - 1:1 Sulfuric acid with H_2O. (3) The tip was found by a "tear drop" method to minimize deformation and provide the desired taper. This consisted of (i) coating the very end of the wire with lacquer and polishing until a neck was produced, (ii) removing the lacquer and polishing until the reduced tip dropped off, (iii) back polishing slightly.

The final process of field evaporation was especially critical for both alloys studied here. Although hydrogen promoted field evaporation was attempted with a number of variations, the number of stable images obtained afterwards was nil. In general the field evaporation rate was too high to control and this invariably led to failure of the tip before obtaining a full image. A more successful method was the field evaporation at room temperature and then at liquid hydrogen temperature with the final imaging gas present.

We were able to attempt a number of imaging gases in our UHV microscope because of the high internal gain available from our internal micro-channel plate intensifier. Briefly the results were that: (1) pure hydrogen was satisfactory for ring solution and specimen symmetry, but gave no point resolution (as expected); (2) pure argon and pure neon gave improved point resolution, but very disordered images (especially the former); (3) pure He gave continous slow field evaporation but good resolution; (4) a mixture of 95% He and 5% Ne gave the most stable image with good resolution, and was used throughout these studies.

Figures 7 and 8 show images of substantially fully ordered Cu_3Au and CnAn obtained by the above procedures. Cu_3Au image developed low index poles [100] and [110] with good point resolutions and higher index poles also developed with reasonable quality. The image was made with 95% He and 5% Ne gas mixture at 21°K tip temperature. Initial image appeared at 7 K.V., however, final form was obtained at 15 K.V. It indicates that there was considerable amount of impurity layers before cleaning off by the field evaporation. A portion of CuAu image is shown in Fig. 8. It shows (001) pole with long period superlattice domain. It is a two phase mixture of CuAu I. and CuAu II. The image was obtained at 10KV with 95% He and 5% Ne mixture.

The micro-channel plate intensifier employed was three inches in diameter, with 40μ channels and proximity focused using 3-4KV post acceleration. It gave a gain of approximately 1000X for 5×10^{-5} Torr of imaging gas and 1000V across the plate. The characteristics of this plate have been described earlier. (19) The high gain permits a substantial reduction in imaging gas pressure 1×10^{-5} Torr and thereby helps to limit the effects of gas impact on field evaporation as well as reducing the required photographic exposure times.

IV. ATOM PROBE

A. Description of Equipment and Testing of Atom Probe

Individual components of the atom probe have been assembled and tested for vacuum and imaging capabilities. The atom probe body is shown in Figure 9. An eight inch flange is located on the top of the atom probe chamber and contains a two and a half inch flange with a semi-rigid bellows to support and position the specimen holder. Also a small liquid N_2 container is mounted on the large flange to enhance the vacuum obtained during operation. The right side of the atom probe body includes another eight inch flange with a centrally located two and one half inch flange that houses the manipulator rod assembly and its flexible bellows. The support structure for this manipulator rod is attached to the outer diameter of the eight inch flange and can be rotated 360 degrees on a roller bearing surface. After the desired initial position is reached, the support assembly is rigidly held in place with three clamps. In order to obtain an accurate final position two micrometers are adjusted to locate the resultant image on the screen and translate individual points of the image to the screen's probe hole.

A four inch diameter view port on the front of the atom probe is located such that a 45 degree tilted front silvered mirror reflects the entire screen image through it. The adjacent one inch view port allows a visual check of the specimen's location within the chamber. If the specimen needs adjustment, the semi-rigid bellows on the top eight inch flange can be altered. The six inch flange on the bottom of the atom probe serves as an an available port for an extra body that includes an evaporating

source, tilted specimen exchange port, vacuum-ion and titanium sublimination pumps. Also located at the bottom of the atom probe chamber is the variable leak valve. This valve is connected to the gas manifold beneath the table top and introduces either hydrogen, helium, argon and neon separately or as mixed components of a mixture into the atom probe.

The two and one half inch port on the left side of Figure 9 supports the internal screen and mirror holder. In addition, it couples the drift tube and Bendix "Channeltron" detector unit with the atom probe chamber. Another semi-rigid bellows is used between the drift tube and the atom probe body to allow two directional motion while aligning the specimen tip with the one millimeter diameter holes in the screen, mirror and drift tube entrance. The "Channeltron" detector is not visible in Figure 9; however, it is located at the end of the drift tube. A strong optical light was used to align the 45 degree tilted "Channeltron" with the one millimeter holes in the screen, mirror and drift tube orifice. Once the drift tube was positioned to give maximum intensity through these holes and another one millimeter hole located at the center of the "Channeltron" cone, the stainless steel tube was locked rigidly into place with two tripods attached to the table top.

Both the drift tube and atom probe body were evacuated to 10^{-9} torr following a 24 hour bakeout at 250°C. An absorption pump is used to rough the system until one of the 20 liter ion pumps can be activated. As the vacuum improves, both 20 liter ion pumps are operated from the same power supply to improve pumping speeds. During imaging the drift tube is isolated from the atom probe body with a UHV right angle valve, except for the one

millimeter hole at the drift tube entrance. By stopping the ion pump in the atom probe chamber and continuing the ion pump in the drift tube, this one millimeter hole enables the drift tube to remain at 10^{-8} torr while the atom probe chamber is at an imaging pressure of approximately 4×10^{-4} torr.

Figure 10 represents a schematic of the atom probe's pulse and "Channeltron" detection circuitry. In order to provide the necessary high voltage pulse to field evaporate the surface atoms, the coaxial high voltage line is coupled with a Microwave Associates Nanosecond Pulser and capacitor. This transmission line is insulated, not sharply bent, and contains as few discontinuities as possible. Following field evaporation the ionic species pass through the screen probe hole to the grounded incident cone of the "Channeltron" detector. As each particle strikes the "Channeltron" surface, secondary electrons are produced and are accelerated to the end of the spiral shaped detector with a +3KV potential. The amount of gain produced by this unit ranges between 10^6 to 10^8. Another +200 volt potential is provided between the end of the "Channeltron" and the collector. When the signal strikes the collector, it travels along a coaxial line through a small blocking capacitor and is fed into the Type 549 Tektronix Storage Oscilloscope.

Testing of the various pulse and detector components was conducted to determine their performance in the completed circuit. Initially, the Microwave Associates Pulser and capacitor were connected to the high voltage line and utilized to field evaporate an iridium specimen. Using a manually controlled pulse with a

2 kv amplitude and 20 nanosecond duration imposed on a 15 kv potential, the iridium tip was observed to be successfully field evaporated. Next, the continuous 60 cps trigger pulse from the Microwave Associates Nanosecond Pulser was observed with the Type 549 Textronix Oscilloscope and connected to this oscilloscope as an external trigger source for the delayed time mode. With the Time Base B set at 2 μsec/cm and a trigger pulse of 1.5 kv amplitude and 2 nanosecond duration, the pulser was manually operated and the individual displays were stored on the oscilloscope as shown in Figure 11a. The displays appear as straight lines over a 20 μsec time period. These results indicate that the Microwave Associates Nansecond Pulser successfully field evaporates the tip and triggers the delayed time mode of the oscilloscope.

The next test involved using the trigger pulse from the Microwave Associates Nansecond Pulser both as the input signal into the oscilloscope's 1A1 preamplifier and as the external triggering source of the delayed time mode. The observed displays are presented in Figure 11 (b). With the total time of the spectrum equalling 50 μsec, one observes that the input signal from the pulser occurred at approximately 35 μsec. When the input signal was introduced from the "Channeltron" detector absent of any applied potential and the delayed time mode was triggered by the pulser, the individual signals appeared similar to Figure 11 (a). This indicates that no spurious signals were introduced in the coaxial lines from the "Channeltron" to the oscilloscope.

Application of a +2 kv potential on the "Channeltron," 2 kv pulse amplitude, +200 v. potential between the exit of the

"Channeltron" and collector and a 15 kv potential on the iridium tip, a spectrum of signals was observed as revealed in Figure 11 (c). The total time span of this display is 10 μsec. Signals are detected at the values of .6, .8, 1.2, 1.6, 2.2, 7.6 and 8.3 μsec and have been identified tentatively as H^+, He^{++}, He^+, N^{++}, N^+, Ir^{++} and Ir^+, respectively.

B. Summary

The atom probe components have been assembled, aligned and are capable of reaching 10^{-9} torr or better and operating in field ionization and emission modes. In addition, the pulser and detector systems appear to function adequately.

REFERENCES

1. Bragg, W. L., (1929), Nature, 143, 678.
2. Ewald, P. P., (1940), Proc. Phys. Soc., 52, 167.
3. Knott, G., (1940), Proc. Phys. Soc., 52, 229
4. Hosemann, R., (1962) Polymer, 3, 349
5. Klug, A., and Buger, M. J., (1950) Acta Cryst., 3, 165.
6. Gould, R. W., private communication.
7. Son, U. T. and Hren, J. J., to appear in Surface Science, vol. 23, Octo. 1970, p. 177.
8. Son, U. T., Ph.D. Thesis (1970), Univ. of Fla.
9. Bragg, W. L. and Williams, E. J. (1934), Proc. Roy. Soc., A145, 699.
10. Cowley, J. M., (1960) Phys. Rev., 120, 5, 1948.
11. Keating, D. T. and Warren, B. E. (1951), J. Appl. Phys., Vol. 22, p. 286.
12. Scott, R. E. (1960), J. Appl. Phys., Vol. 31, 12, p. 2112.
13. Nagy, I. (1965), J. Phys. Chem. Solids, Vol. 26, p. 179.
14. Chipman, D. R. (1956), J. Appl. Phys., Vol. 27, p. 739.
15. Airoldi, G. and Asdente, M. (1969), Phys. Stat. Sol. 32, p. 691.
16. Turner, P. J. and Southon, J. M. (1969), 16th Field Emission Symposium.
17. Ralph, B. et. al. (1969) 16th Field Emission Symposium.
18. LeFevre, B. G. (1970) to be appearing Oct. issue of Surface Science.
19. Son, U. T. and Hren, J. (1969), 16th Field Emission Symposium.

Table I

	A	B	C	D	E	F	G	H	I	J	K	L	M	N	O	P	Q	R
A	-																	
B	3.5	-																
C	4.5	5.9	-															
D	5	4.4	2.9	-														
E	6.6	4.0	6.1	3.3	-													
F	8.7	10.6	4.7	7.0	10.3	-												
G	8.2	9.1	3.7	4.9	7.8	3.0	-											
H	8.2	8.1	4.2	3.7	5.9	5.5	2.5	-										
I	9.1	7.8	6.1	4.1	4.4	8.3	5.3	2.8	-									
J	10.8	8.5	8.9	6.3	4.5	11.7	8.8	6.3	3.4	-								
K	13.4	14.8	9.1	10.7	13.4	4.8	5.7	7.6	10.1	13.4	-							
L	12.5	13.3	8.0	8.9	11.3	5.1	4.3	5.4	7.5	10.7	2.9	-						
M	12.2	12.3	7.9	7.9	9.7	6.4	4.4	4.2	5.6	8.4	5.4	2.5	-					
N	12.5	11.8	8.6	7.6	8.5	8.6	6.0	4.4	4.1	6.1	8.3	5.4	2.8	-				
O	14.0	12.5	10.9	9.1	8.5	12.0	9.2	7.0	5.0	4.5	12.0	9.0	6.5	4.7	-			
P	16.4	16.7	12.0	12.3	14.0	9.3	8.3	8.5	9.7	12.0	5.8	4.2	4.3	5.9	8.8	-		
Q	16.8	16.3	12.6	12.1	13.0	11.2	9.3	8.5	8.6	10.1	8.6	6.3	4.8	4.5	6.1	3.4	-	
R	21.2	20.0	17.4	16.2	16.2	16.8	14.6	13.2	12.3	12.1	14.4	12.1	10.3	8.8	7.7	8.9	5.8	-

TABLE II

Comparison of the long range order parameters obtained by theories and different experimental techniques for FePt alloy (Llo Type super lattice)

S / T/Tc	Theories		Experimental		
	Bragg & Williams	Cowley	X-Ray	F. I. M.	
				Direct Count.	Optical Trans.
.95	0.32	0.55	0.55	0.65	0.62
.90	0.47	0.70	0.72	0.79	0.77
.89	0.98	0.79	0.79	0.89	0.83
.80	0.66	0.83	0.85	0.91	0.88
.75	0.75	0.90	0.90	0.94	0.91
.70	0.82	0.91	0.91	0.96	0.93
.65	0.86	0.96	0.96	0.97	0.94
.60	0.91	0.97	0.97	0.98	0.95
.55	0.93	0.98	0.97	0.99	0.95
.50	0.96	0.98	0.98	0.99	0.95

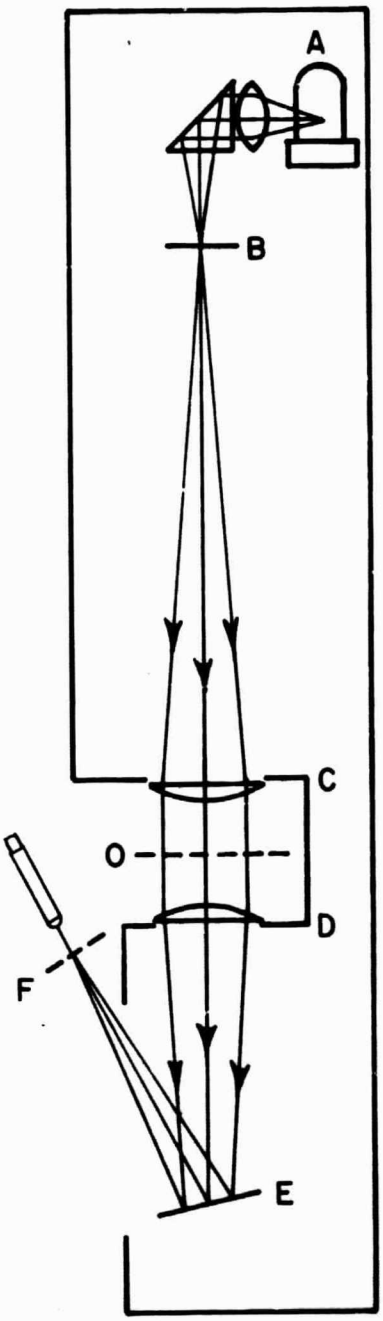

Fig. 1. The general arrangement of the optical diffractometer showing the beam path.

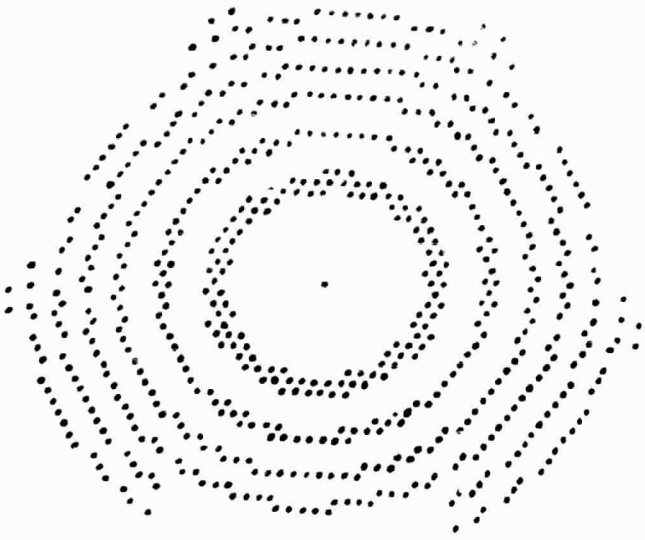

(a)

(b)

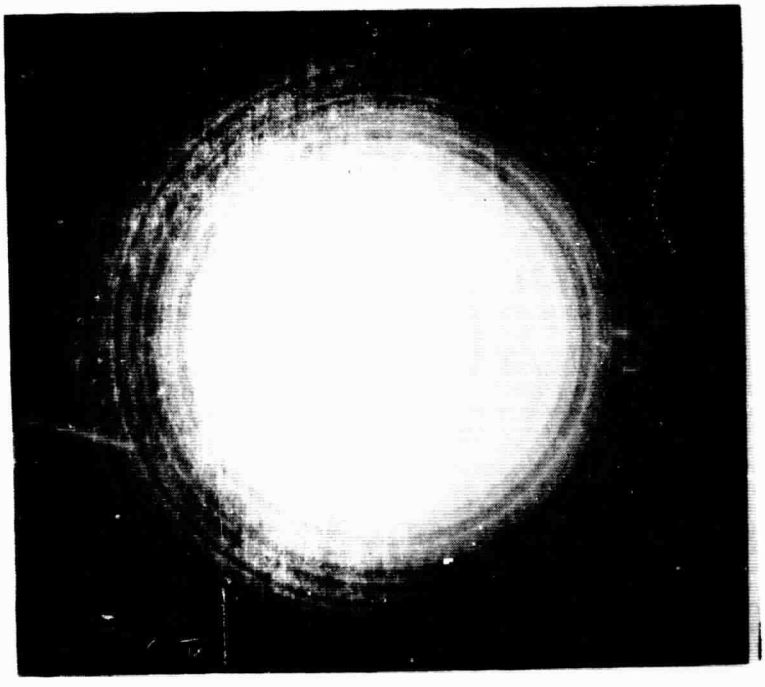

(c)

Fig. 2. (a) An ideal mask for a computer simulated field-ion micrograph. (b) Stational diffraction pattern of (a). (c) Rotational diffraction pattern of (a).

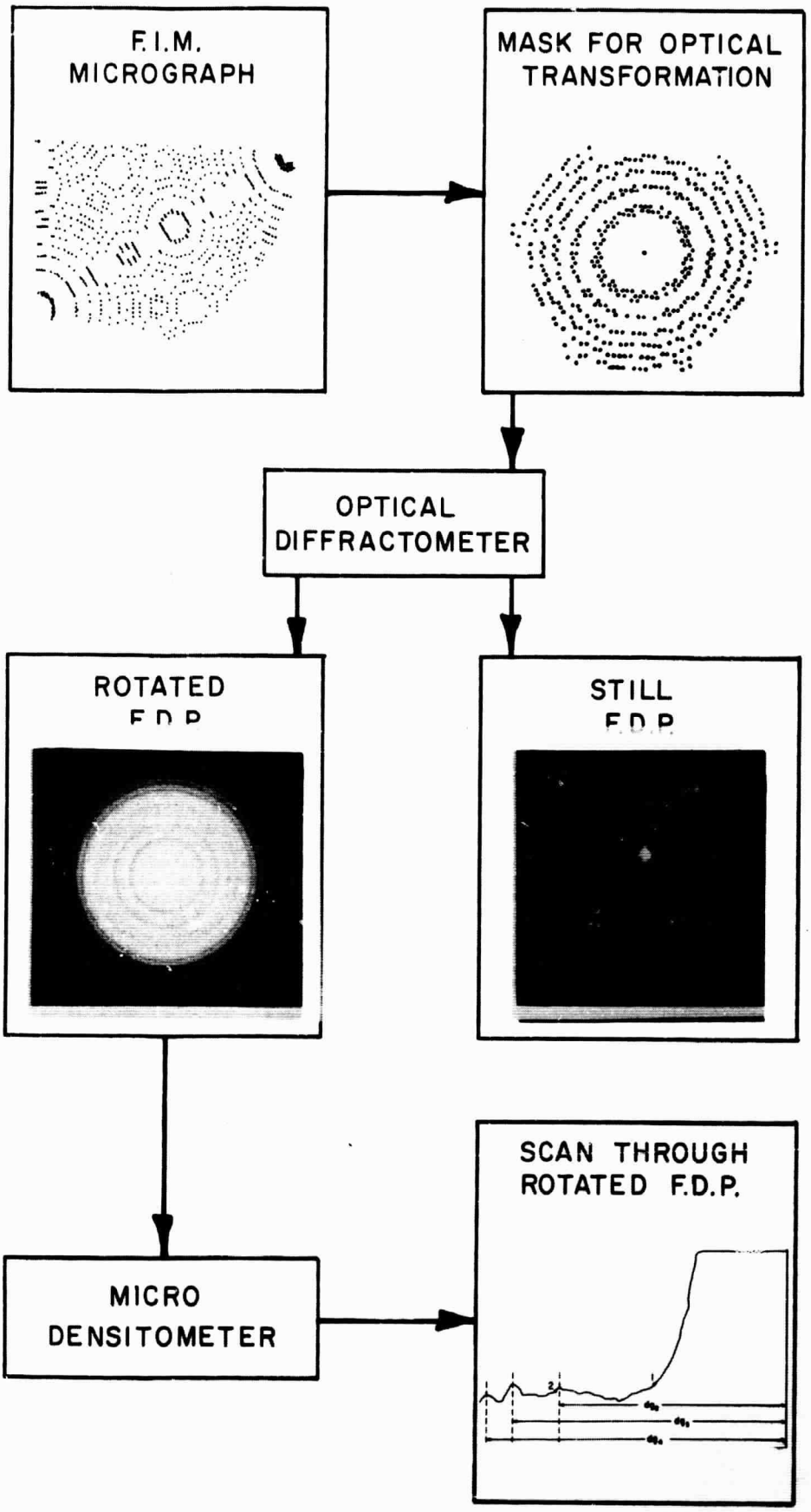
F.I.M.
MICROGRAPH
MASK FOR OPTICAL
TRANSFORMATION
OPTICAL
DIFFRACTOMETER
ROTATED
STILL
MICRO
DENSITOMETER
SCAN THROUGH
ROTATED F.D.P.

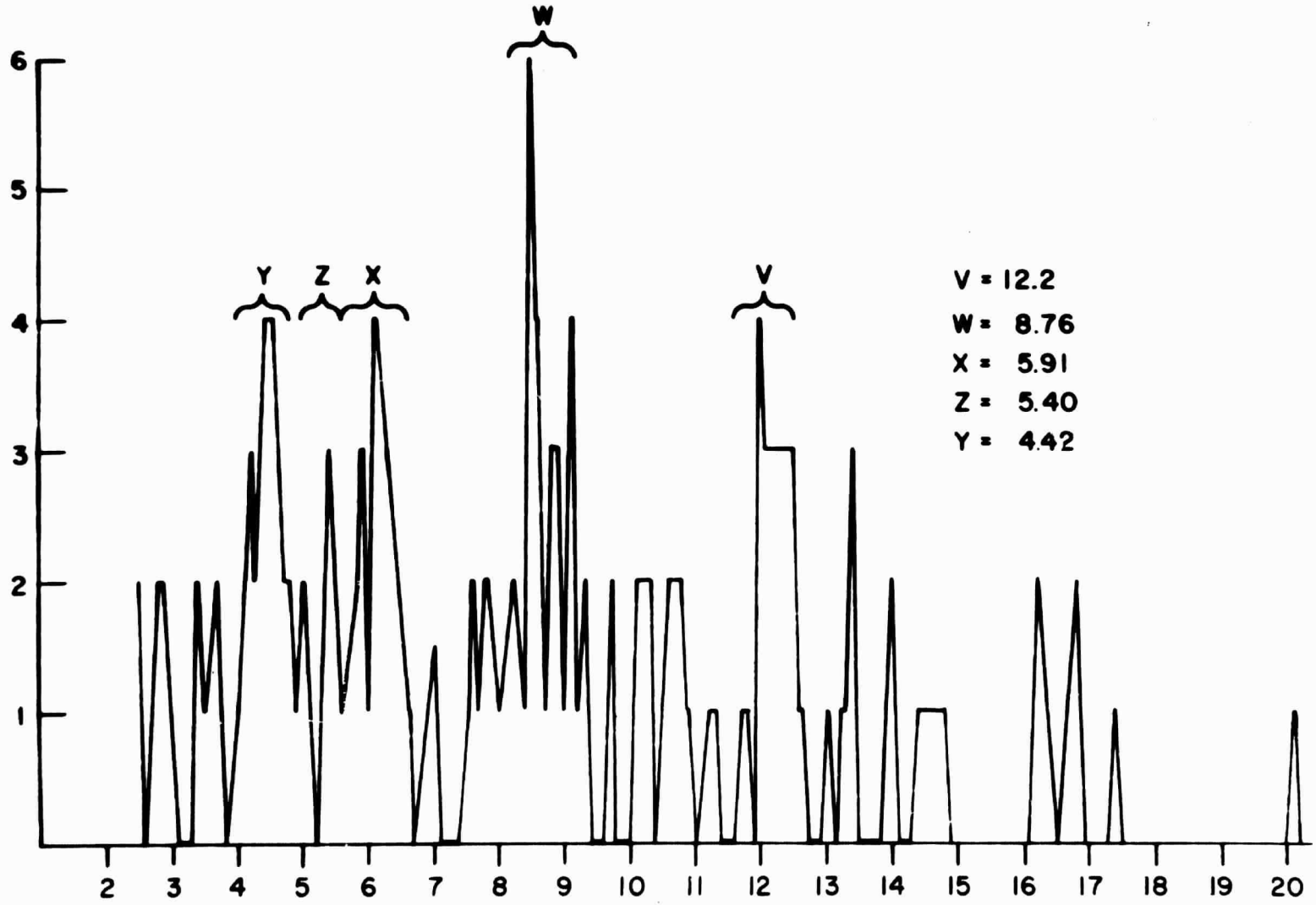

Fig. 3. Point group distribution chart. Plotting of the image point separation versus frequency.

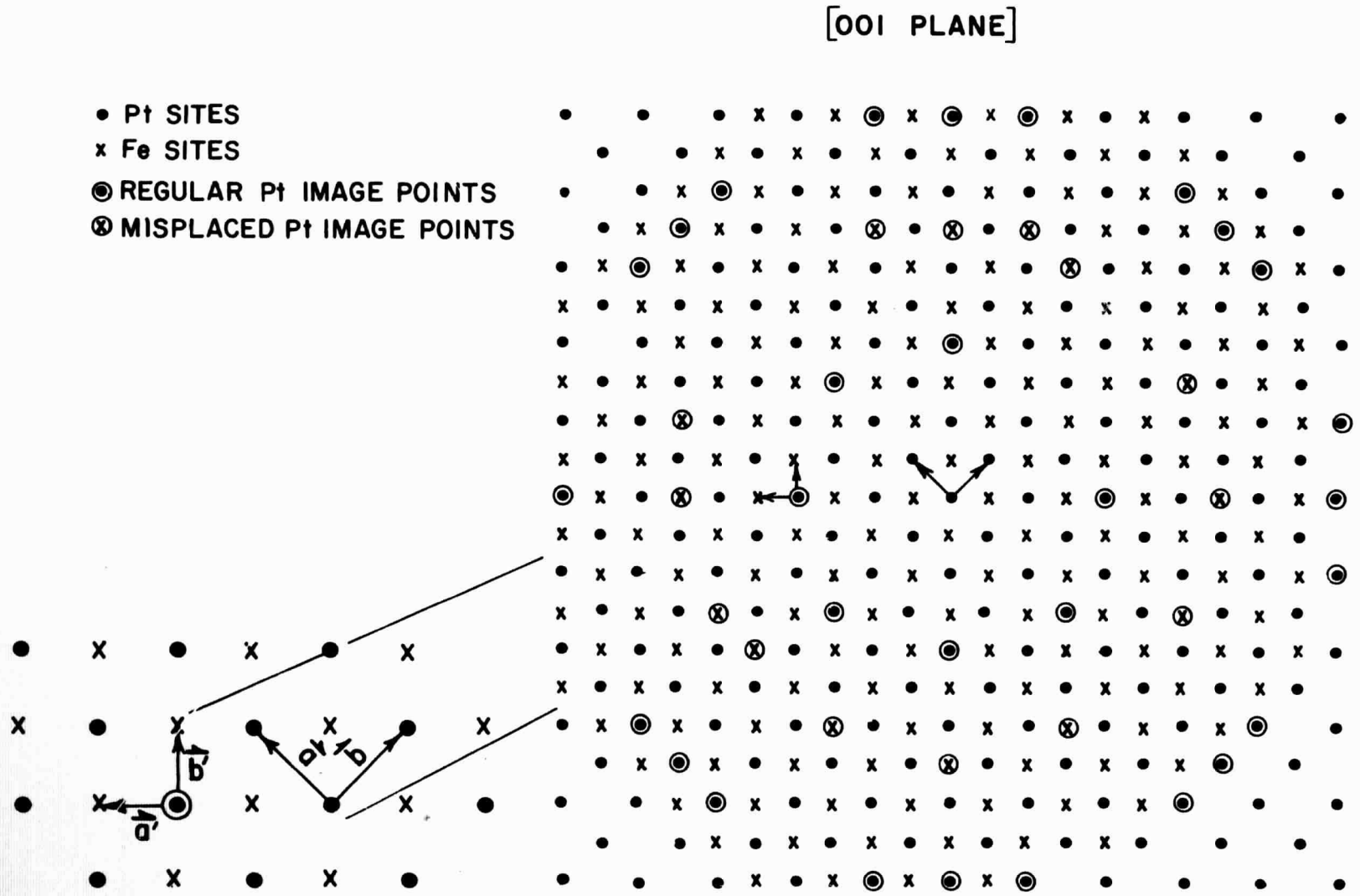

Fig. 4. Schematic drawing showing the relationship between field-ion image points and the lattice sites for $L1_0$ type super lattice.

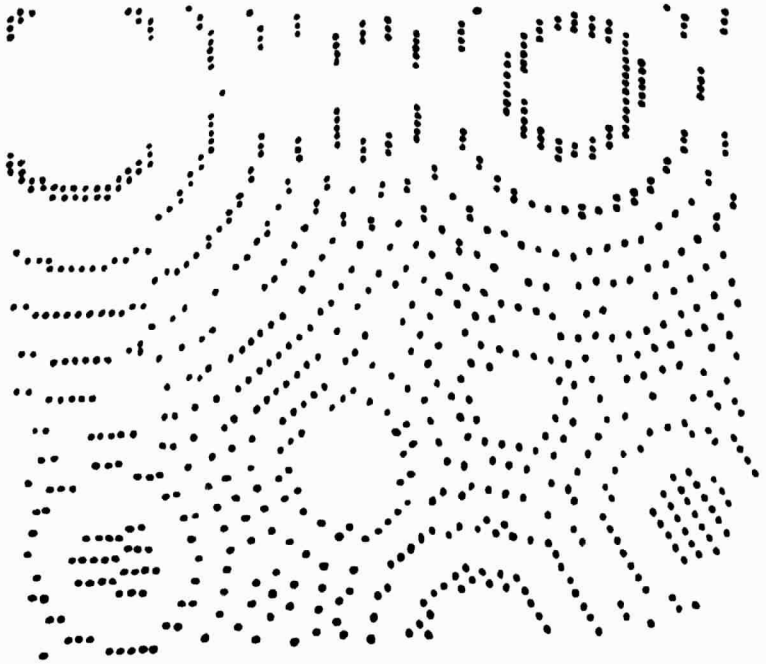

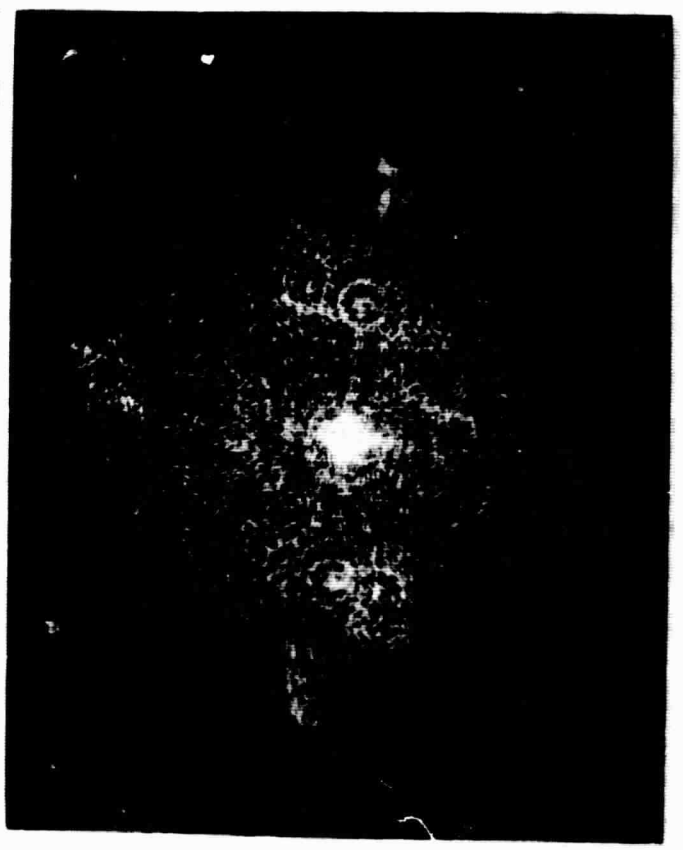

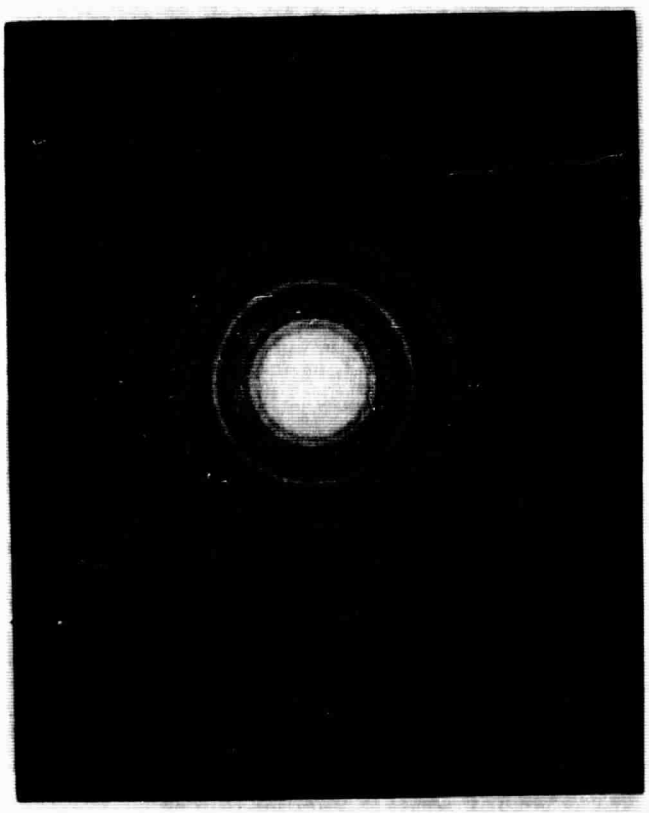

Fig. 5(a) A computer simulated field-ion image with corresponding stationa! and rotational optical diffraction patterns.

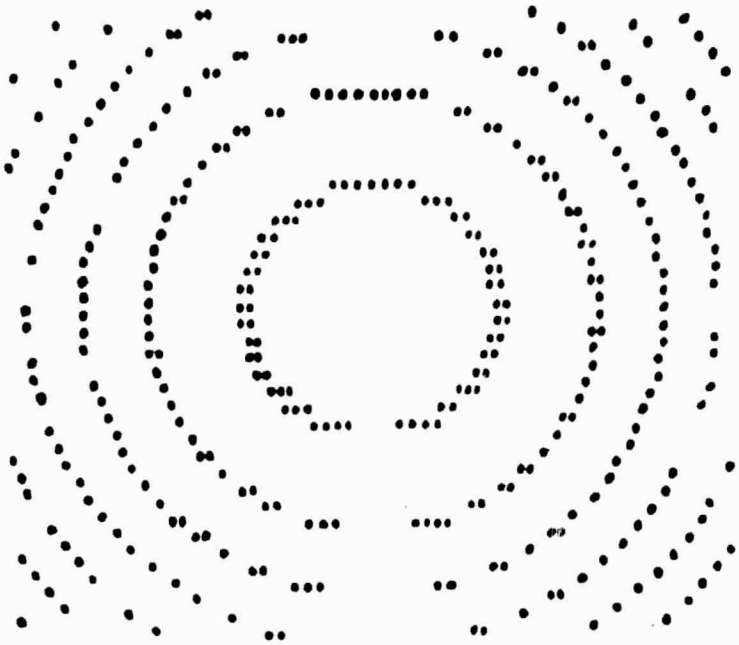

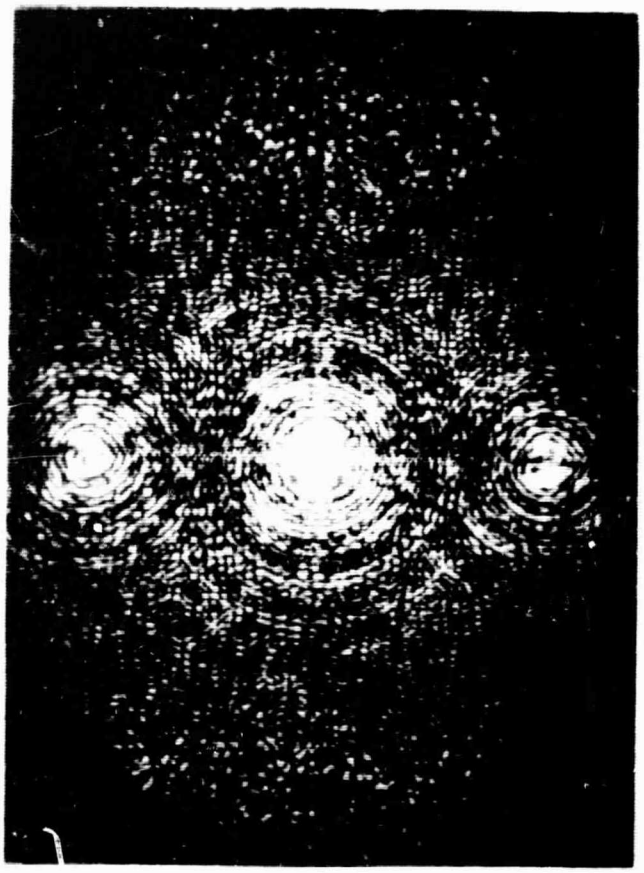

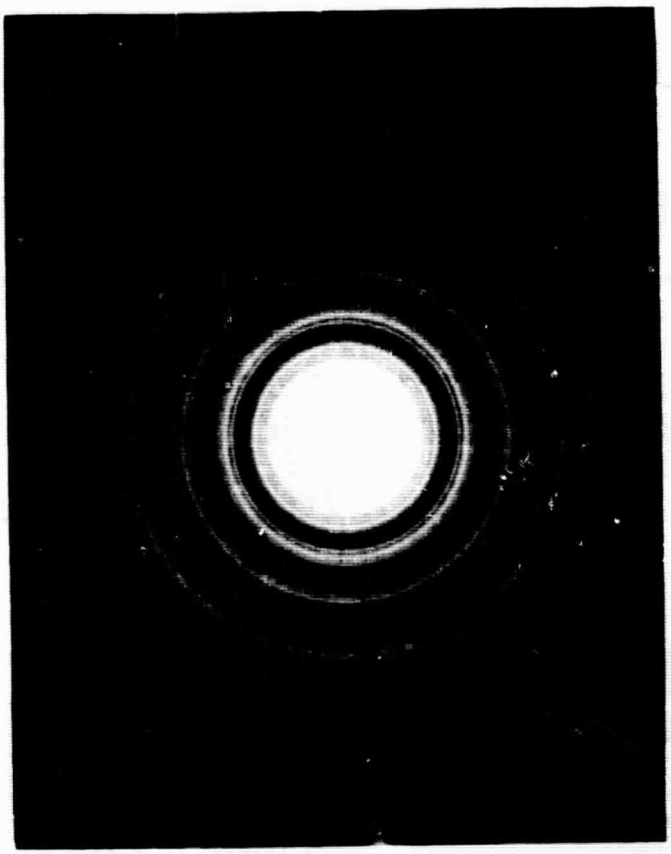

Fig. 5(b) A computer simulated field-ion image with corresponding stational and rotational optical diffraction patterns.

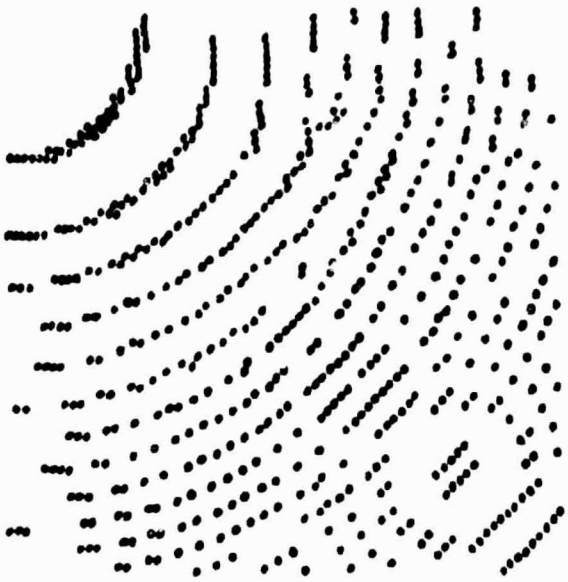

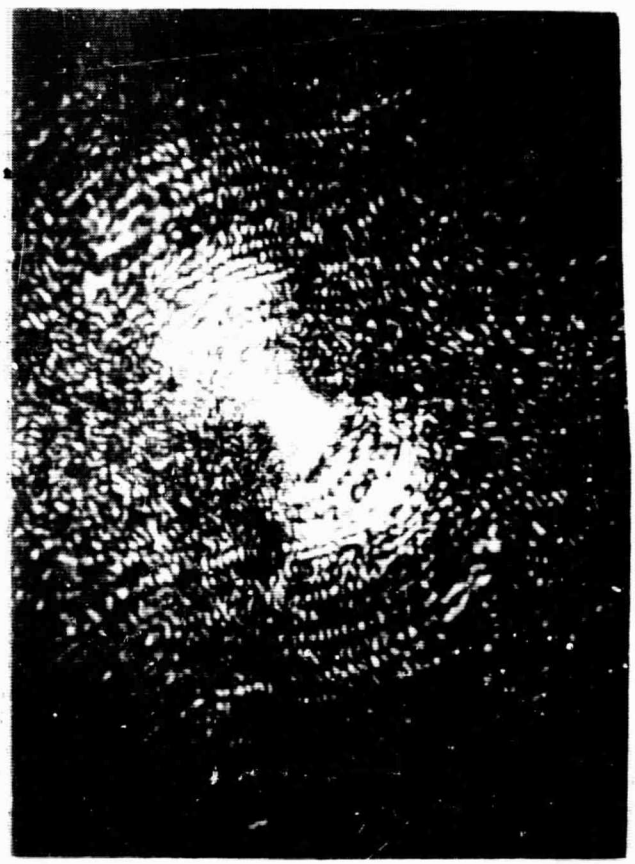

Fig. 5(c) A computer simulated field-ion image with corresponding stational and rotational optical diffraction patterns.

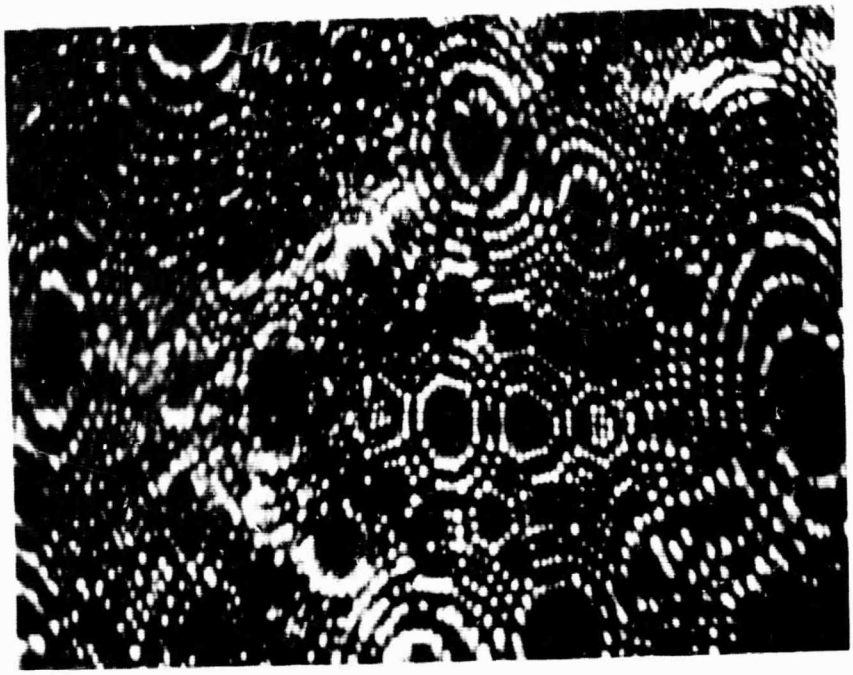

(a)

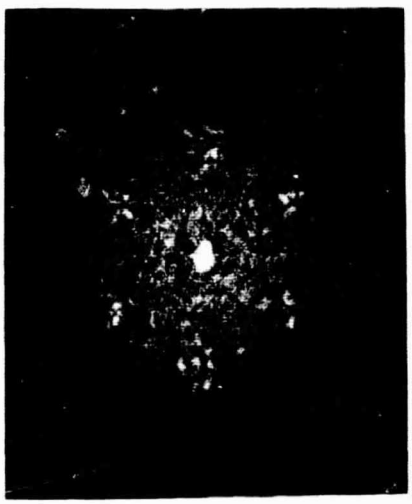

(b)

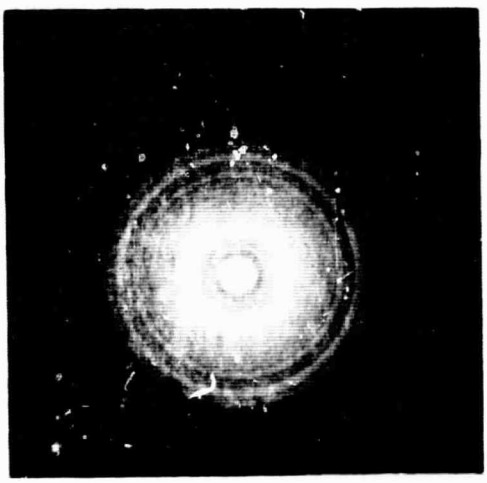

(c)

Fig. 6. (a) An actual field-ion micrograph
(b) Stational diffraction pattern of (a).
(c) Rotational diffraction pattern of (a).

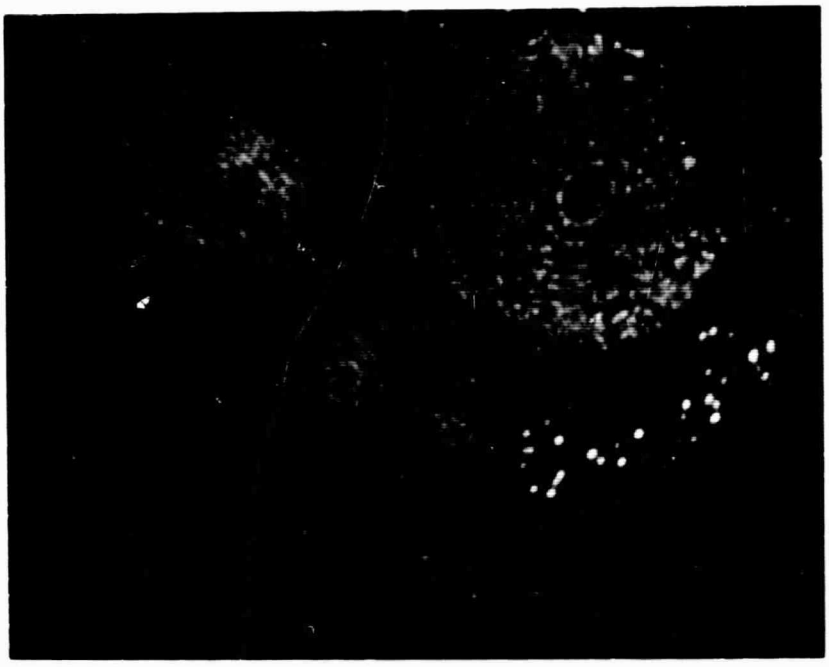

Figure 7. Field-ion micrograph of ordered Cu_3Au. Imaged at 15 KV with 3" Bendix channel plate image intensifier, and helium image gas of 5 X 10^{-5} torr at 21°K.

Figure 8. Field-ion micrograph of AuCu showing two phases of AuCu I and AuCu II. The parallel lines are AuCu II with long period anti-phase domain boundaries. Imaged at 10 KV with 3" Bendix channel plate image intensifier and helium image gas of 5 X 10^{-5} torr at 21°K.

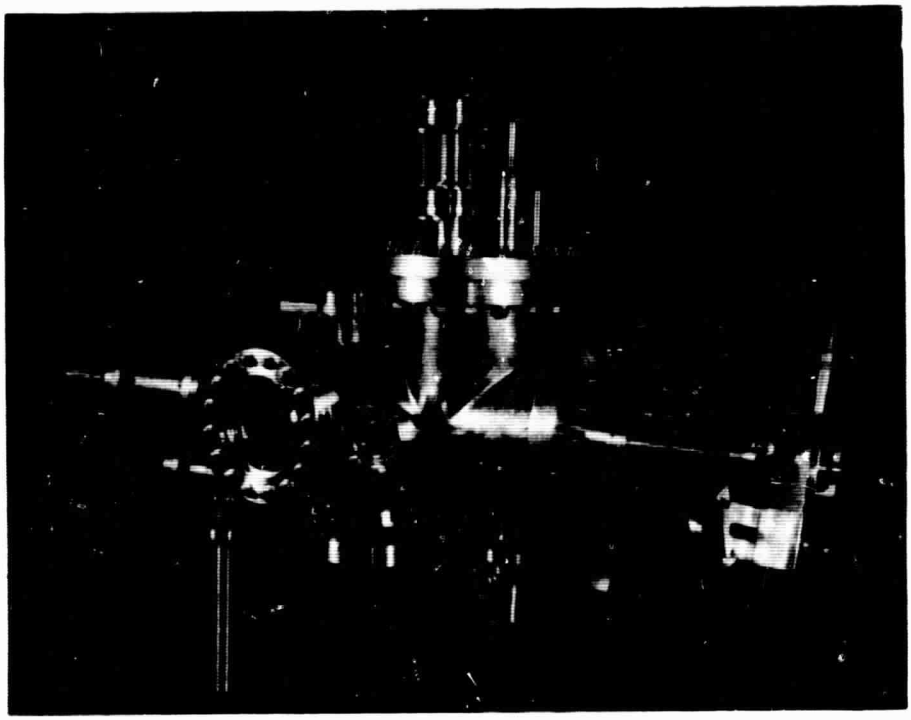

Figure 9. Assembled Atom Probe Body.

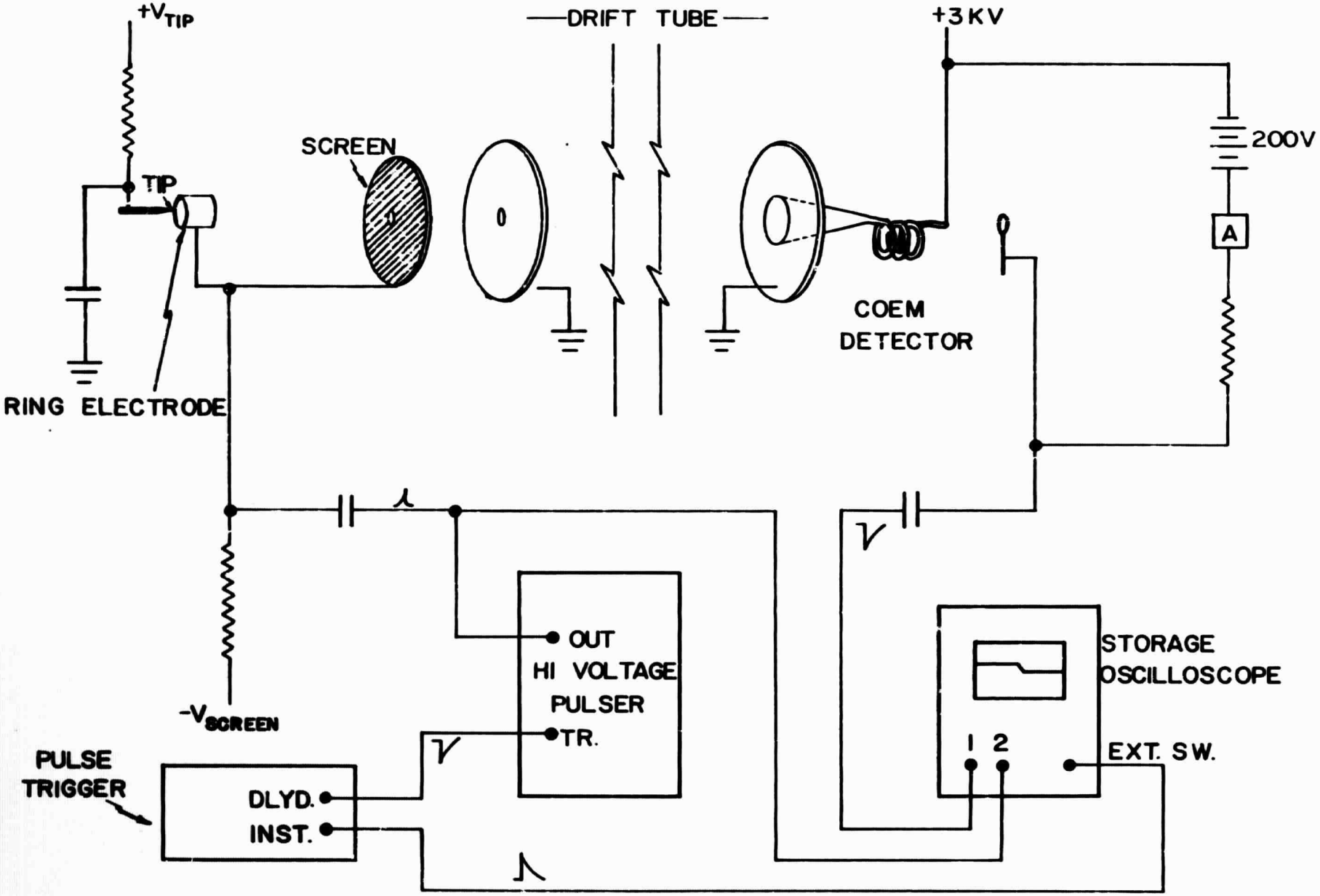

FIGURE 10. ATOM PROBE PULSE & DETECTION SCHEMATIC

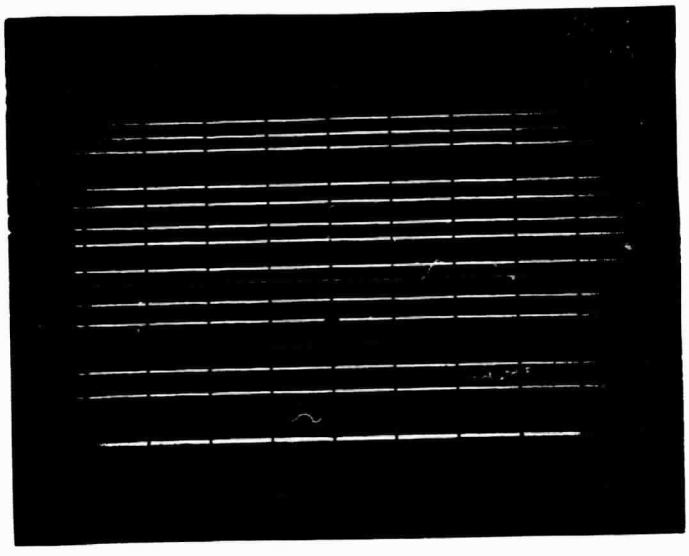

(a)

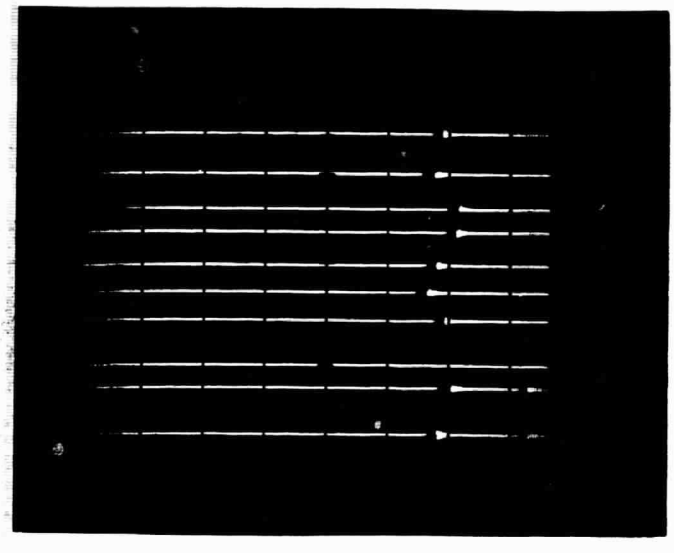

(b)

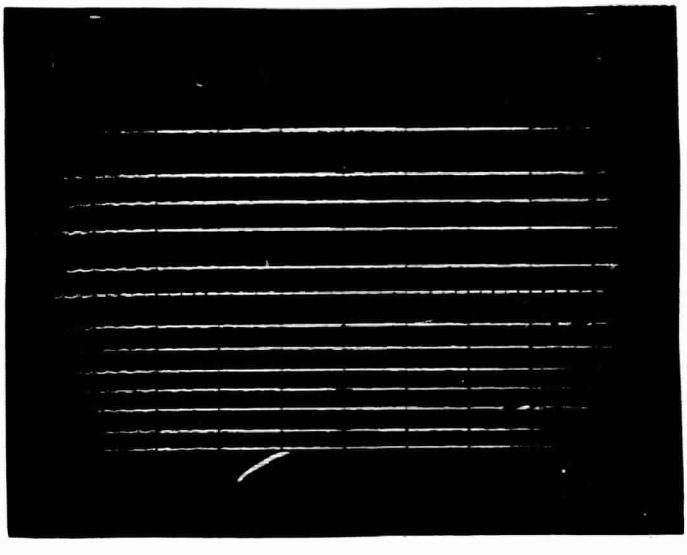

(c)

Figure 11. Displays From Storage Oscilloscope.